

RESEARCH ARTICLE

10.1002/2014JD021905

Key Points:

- Passively obtained infrasound recordings can be used to probe the stratosphere
- Observed amplitude variations reveal details on the life cycle of a SSW
- Amplitudes variations allow to estimate the return height

Supporting Information:

- Readme
- Figure S1
- Figure S2
- Figure S3
- Figure S4
- Figure S5
- Figure S6

Correspondence to:

P. S. M. Smets,
pieter.smets@knmi.nl

Citation:

Smets, P. S. M., and L. G. Evers (2014), The life cycle of a sudden stratospheric warming from infrasonic ambient noise observations, *J. Geophys. Res. Atmos.*, 119, 12,084–12,099, doi:10.1002/2014JD021905.

Received 18 APR 2014

Accepted 10 OCT 2014

Accepted article online 14 OCT 2014

Published online 13 NOV 2014

The life cycle of a sudden stratospheric warming from infrasonic ambient noise observations

P. S. M. Smets^{1,2} and L. G. Evers^{1,2}

¹Seismology Division, Royal Netherlands Meteorological Institute (KNMI), De Bilt, Netherlands, ²Department of Geoscience and Engineering, Faculty of Civil Engineering and Geosciences, Delft University of Technology, Delft, Netherlands

Abstract A method is presented to study the life cycle of a SSW using infrasonic ambient noise observations. The potential of infrasound is shown to provide the missing observations required by numerical weather prediction to better resolve the upper atmosphere. The 2009 major SSW is reanalyzed using the Evers and Siegmund (2009) data set. Microbarom observations are evaluated to identify detections that cannot be explained by the analysis of the European Centre for Medium-Range Weather Forecasts. Identified differences can be related to either the altitude limit of the analysis, not resolving thermospheric ducts, or to an actual error in the analysis. Therefore, a first-order model is used to relate observations with the analysis, existing of the Waxler et al. (2007) microbarom source model, including bathymetry to allow column resonances, and an atmospheric propagation model using 3-D ray tracing. Daily normalized spectral powers are proposed to distinguish stratospheric from thermospheric return height, based on the different signature of solar tidal amplitude fluctuations. It is shown that a SSW is not a smooth event as following from the analysis but a series of abrupt changes with a period of 10 to 16 days, increasing in intensity and duration. This is in agreement with the wave period of Rossby waves, interacting with the stratospheric circumpolar vortex. The type of vortex disturbance, split or reversal, can be deduced from the combined effect of the change in back-azimuth direction, solar tidal signature type, and/or phase variation of the amplitude variation of the observed microbaroms.

1. Introduction

An optimal estimate of the true state of the atmosphere, called the analysis, is widely used in many fields of research. The analysis is a product of the data assimilation system, given as input a set of observations and a first-guess field. The first-guess field is defined by the time integration of the model equations from the previous analysis. A good analysis, which is what everyone desires, requires both a good model and good observations. However, observations can be problematic, because a lot of them are required (in space and time) with resemblance with the model itself. If observations deviate too much from the first-guess, they are neglected.

Improving forecasts involves resolving the stratosphere and assimilating upper atmospheric data [Ramaswamy et al., 2001; Gerber et al., 2009]. Stratospheric and lower mesospheric temperature observations are dominated by Advanced Microwave Sounding Unit type A (AMSU-A) observations, available by more than a dozen satellites, and are directly assimilated in, e.g., the European Centre for Medium-Range Weather Forecasts (ECMWF) models.

In the stratosphere, global circulation is derived from only these temperature observations. The stratospheric circumpolar vortex is driven by a temperature gradient between the equator and the poles, resulting from the unequal solar insolation. The seasonal variation in the atmosphere's heat balance changes the direction of the circumpolar vortex around the vernal and autumnal equinoxes. For this induced circulation, the Coriolis force balances the acceleration due to moment flux convergence to maintain the thermal-wind balance [Muench, 1965]. In summer, the circumpolar vortex is easterly, characterized by a stable stratospheric wind and temperature structure. In winter, however, the westerly circumpolar vortex is stronger but unstable. The latter is essentially the topographically induced instability of Rossby waves due to the conservation of the planetary vorticity [Chao, 1985]. This instability allows midwinter Sudden Stratospheric Warmings (SSWs), occurring approximately twice every 3 years Charlton and Polvani [2007]. Within a weak the stratospheric temperature, poleward from 60° latitude, increases 25°C resulting in dramatic changes of the circumpolar vortex [McInturff, 1978]. SSWs are generated by an enhanced vertical propagation of

planetary waves, consisting primarily of zonal wave numbers 1 and 2, from the troposphere into the stratospheric polar vortex [Matsuno, 1971; Andrews *et al.*, 1987; Kodera *et al.*, 2013]. When the winter stratospheric polar vortex is triggered by the planetary scale disturbances, eddy potential vorticity flux is deposited in the stratosphere, reducing the pole-to-equator mean temperature gradient [Charney and Drazin, 1961]. As the wind zonal-mean flow is to remain geostrophic, the thermal wind must decrease as well. The stratospheric polar vortex gets highly distorted and will eventually break down. Due to this large-scale phenomena, a SSW is the primary atmospheric variation, being the clearest and strongest proof of the dynamical coupling between the stratosphere and troposphere [Charlton and Polvani, 2007; Shaw and Shepherd, 2008]. The slow recovery of the polar vortex in the lowermost stratosphere following an SSW is able to influence the troposphere at long lags up to 30 days [Gerber *et al.*, 2009]. AMSU-A is capable of capturing the fast temperature variations related to the SSW. But due to the very rapid changes, the first-guess field and observations differ significantly resulting in a possible rejection of all AMSU-A data. Consequentially, the quality of the analysis, and thus the forecast, will reduce. To improve the analysis in times of a SSW, additional upper atmospheric observations are required.

Infrasound, used as a verification technique for the Comprehensive Nuclear-Test-Ban Treaty (CTBT), has shown its ability to act as a passive remote sensing technique to probe the upper atmosphere [Donn and Rind, 1971; Le Pichon *et al.*, 2010; Green *et al.*, 2012; Assink *et al.*, 2012]. Infrasound propagates through the atmosphere, up to thermospheric altitudes, retaining information on the whole atmosphere in the passive observations at the surface [Drob *et al.*, 2003]. Previous studies have shown that infrasound can be used to monitor the seasonal change in direction of the stratospheric polar vortex around the equinoxes by looking at signals arriving from the opposite direction [Garcés *et al.*, 2004; Landès *et al.*, 2012] or changes in mean amplitude variations of ambient coherent noise [Rind and Donn, 1978]. Stratospheric changes of wind dedicated to a SSW can be monitored similarly, by looking at signals arriving from the opposite direction than expected under regular winter conditions [Evers and Siegmund, 2009; Hedlin *et al.*, 2010], or by looking at simultaneous arrivals from two stratospheric ducts [Assink *et al.*, 2014]. Evers *et al.* [2012] studied the temperature effect of a hot stratosphere during a SSW on infrasound propagation, observing the shadow zone. During a SSW, the extent of the classical stratospheric shadow zone (~200 km) reduces by a factor of 2, leading to extremely small shadow zones. As infrasound has clearly shown its potential in probing the upper atmosphere, with clear signatures of a SSW, it is not yet used, or known, for numerical weather prediction (NWP). So, in what extend can infrasound now contribute to NWP to better resolve a SSW?

Therefore, the 2009 SSW data set of Evers and Siegmund [2009] is reanalyzed to identify trends in infrasound ambient noise observations, due to a coherent signal from a finite source region in the oceans, that cannot be explained by the ECMWF analysis. Microbaroms are atmospheric pressure oscillations, radiated from ocean surface wave-wave interaction at double the ocean surface wave frequency [Gutenberg, 1939; Longuet-Higgins, 1950]. Large regions of high-energetic ocean waves, e.g., ocean swell and marine storms, radiate almost continuously acoustic energy well characterized by a radiation frequency of 0.2 ± 0.1 Hz. Because microbaroms vary in space and time, a source model is required. Microbaroms can be modelled using a two-fluid model, over air and seawater, and an ocean-atmosphere model providing the sea state [Waxler and Gilbert, 2006]. The Waxler and Gilbert [2006] finite ocean microbarom radiation source model has been validated by Walker [2012] and Stopa *et al.* [2012], studying ambient swell and hurricane induced microbaroms, respectively. In this study, the Waxler *et al.* [2007] finite ocean microbarom radiation source model is used, not yet validated, which takes into account the effect of resonance due to bathymetry affecting the source location, amplitude, and frequency. The data set of Evers and Siegmund [2009] is limited to only the Arctic infrasound observations, containing the clearest infrasonic signature, to clarify this study. Similar analyses of more recent winters, using the same infrasound arrays, are made available as supporting information.

The article is organized as follows. The data used are explained in section 2. The microbarom source model, atmospheric propagation model, and their combination to simulate the microbarom observations are described in section 3. The results of the observations, microbarom source model, and the simulations are presented in section 4. In this section, additional analysis is performed to determine the atmospheric return height using only observed amplitude variations. Section 5 explains the life cycle of the 2009 SSW. Finally, discussion and concluding remarks are given in section 6.

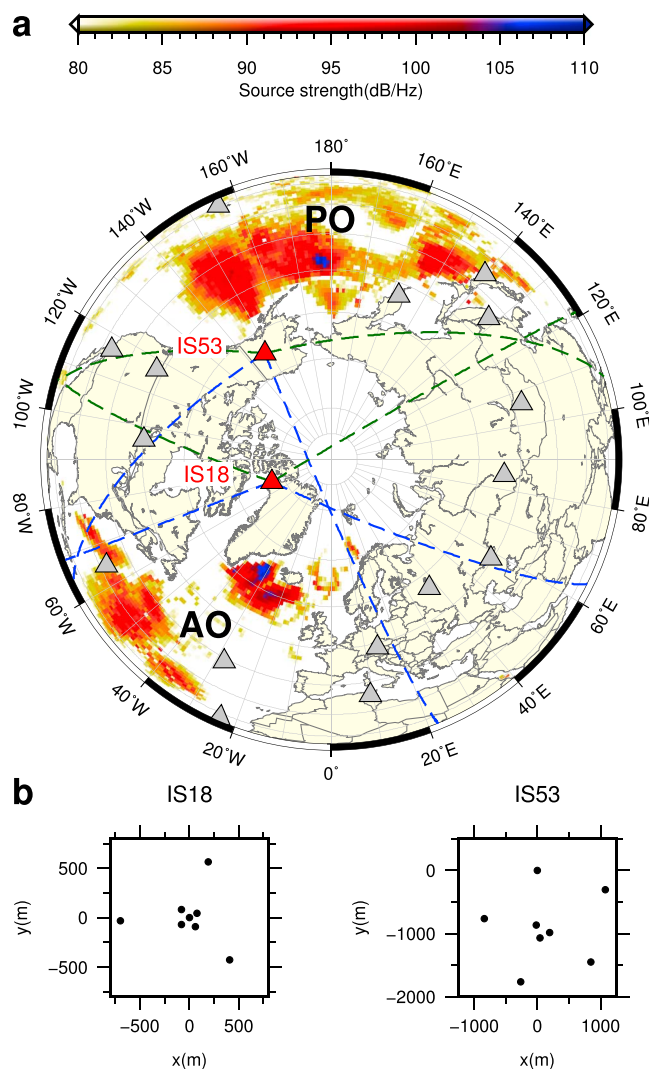


Figure 1. Map of infrasound arrays of the IMS for the verification of the CTBT on the Northern Hemisphere at latitudes higher than 15°N. (a) Red triangles indicate the locations of the two (near) Arctic arrays used, IS18 and IS53, respectively. Grey triangles correspond with the remaining certified IMS infrasound locations for the period of the warming. Colour coded are the microbarom amplitudes in the Atlantic and Pacific Ocean corresponding to 2009, 19 January at 12 UT, applying the *Waxler and Gilbert* [2006] model including bathymetry [Waxler et al., 2007]. Dashed lines indicate the used back-azimuth limits of the arrays toward to AO (blue) and PO (green). (b) The geometrical configurations of arrays IS18 and IS53 are given in the two bottom frames.

2. Data

2.1. Arctic Infrasound Observations

Three months of infrasound recordings, from December 2008 to February 2009, of two (near) Arctic infrasound arrays is used. These stations are in place for the verification of the Comprehensive Nuclear-Test-Ban Treaty (CTBT) and are part of the International Monitoring System (IMS). The IMS is a global network providing infrasound, seismic, hydroacoustic, and radionuclide recordings, designed to detect and locate nuclear explosions in the atmosphere, ocean, and solid earth [Dahlman et al., 2009]. Infrasound is recorded using arrays, consisting of at least four microbarometers. The sensors have a flat frequency response in the pass band from 0.02 to 4 Hz and are sensitive for amplitudes of several mPa up to tens of pascals. Pressure fluctuations are sampled at 20 Hz. In 2009, two out of three (near) Arctic IMS infrasound arrays were operational: IS18DK in Qaanaaq, Greenland (77.5°N 69.3°W), and IS53US in Fairbanks, Alaska (64.9°N 147.9°W). The station layouts and locations of the two operational stations are provided in Figure 1. Both arrays consist of eight elements and have an aperture of 1170 and 1980 m, respectively. The layout is designed such that the array response function has a circular response for the desired frequency range and suppresses unwanted side lobes to avoid spatial aliasing. To reduce wind noise, each array element is connected to a passive wind noise reduction system. This is a series of pipes with discrete inlets, spatially integrating the pressure field to increase the signal-to-noise ratio [Hedlin et al., 2003; Walker and Hedlin, 2009].

Signals are filtered using a second-order Butterworth band-pass filter with corner frequencies of 0.1 and 0.5 Hz. Possible detections, coherent signals, are obtained applying the Fisher ratio (F) in the time domain [Melton and Bailey, 1957] with a moving window of 12.8 s (256 samples) with 50% overlap between successive windows. The Fisher ratio provides an estimate of the detection probability and is related to the signal-to-noise-ratio (SNR) assuming normal distributed uncorrelated noise: $F = 1 + N \cdot SNR^2$, with N the number of array elements. The slowness grid for the beamforming is defined from 0 to 360° for back-azimuth (ϕ) and from 250 to 500 $m s^{-1}$ for apparent velocity (c_{app}) with steps of 1° and 5 $m s^{-1}$, respectively. For each time window 18,360 beams are examined. Subsample time shifts are obtained by bicubic interpolation of the time signals. The maximum value of F corresponds to the best-beam and a possible

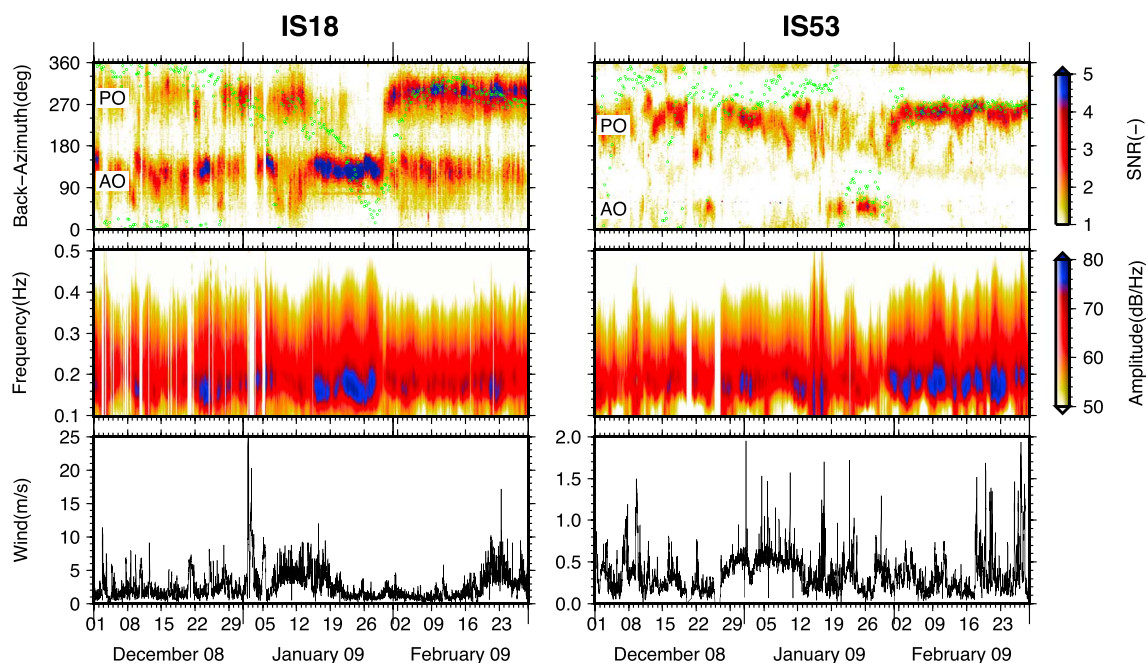


Figure 2. From top to bottom are shown array processing results and wind observations at the array side for IS18 (left) and IS53 (right), respectively. (top) The maximum hourly signal-to-noise ratio (*SNR*) for each back-azimuth direction per hour as derived from the Fisher analysis. Only events with a *SNR* > 1 are used. The green dots represent the wind direction at 50 km altitude above the array, derived from the ECMWF HRES analysis model. (middle) The energy spectrum, averaged per hour. (bottom) The wind measured at the array site, low-pass filtered for a period of one hour.

detection. Let F_ϕ be the maximum F for each back-azimuth angle ϕ . Multiple detections per time window are allowed by determining the local maxima of F_ϕ , applying a 1-D peak detection algorithm. For each detection, the time signals of all sensor are aligned, based on the array response travel time delays, and averaged to obtain the best-beam signal. The energy spectrum or amplitude spectral density (ASD) of each best-beam with a length of 204.8 s (4096 samples) is determined by applying the fast Fourier transform (FFT) and a flat top taper window to correct for amplitude leakage due to the finite signal. As the determination of the atmospheric return heights (see subsection 4.2) makes use of variations in the observed spectral amplitudes, a shorter time window is used. The use of a much longer time window for the spectral analysis than for the beamforming ($4096 \gg 256$ samples) can result in an error in the array processing results, as the best-beam can include signals that can influence the *SNR*. For the energy spectrum shown in Figure 2, this is not a problem, as all directions are averaged for each hour. For the determination of the atmospheric return height, based on the spectral power, it is important as the signals of the AO and PO are separated. For the analysis of the observed amplitudes to determine the return height, the beamforming time window is used, 256 samples, elongated up to 4096 samples by adding zeros. This is done to achieve enough spectral resolution, while minimizing the error of including false signals.

2.2. Ocean Wave Data

The European Centre for Medium-Range Weather Forecasts (ECMWF) high-resolution Ocean Wave Model (WAM) is used as a sea state model for microbarom modelling (Cy35r1, September 2008), consisting of both model data and assimilated buoy and satellite data. The WAM model is coupled to the ECMWF atmosphere model (WAM HRES). This allows interaction between the ocean waves and the surface winds, which is important for microbarom simulations. The sea state is described by the 2-D wave spectra (2DFD), consisting of 30 steps for frequency and 24 for direction, respectively. Integration of the 2-D wave spectra over direction and frequency results in the significant wave height for each longitude and latitude. Wave periods (T) range from approximately 28.5 s down to 1.8 s, varying logarithmically ($T_0/T_n = 1.1^{n-1}$), with a maximum horizontal resolution of 0.36° [Ecmwf, 2009]. 2DFD are available every 6 h, globally, with latitudes up to 85° .

2.3. Atmospheric Specifications

Atmospheric specifications, the analysis, are obtained from the ECMWF High-Resolution Atmospheric Model (HRES, Cy35r1, September 2008) making use of the Integrated Forecast System (IFS). It is a global circulation

model consisting of assimilated radiosonde, ground, and satellite based atmospheric observations by four-dimensional variational assimilation (4D-Var). HRES exists of 91 levels with a horizontal resolution of T799 (~25 km) up to 0.01 hPa (~78 km). Analyses are available every 6 h. For this study, 6-hourly atmospheric specifications of wind (zonal, meridional, and vertical), temperature, humidity, and pressure are used with a grid resolution of 1°. The two upper levels are neglected. Those levels operate as a sponge layer, filtering wave reflections, which is required for model stability but provides an unrealistically representation of the atmosphere. Therefore, the maximum altitude is limited to 70 km. This is much lower than the thermospheric return height (~120 km). Consequentially, thermospheric signals cannot be resolved using the ECMWF analysis.

3. Model

3.1. Microbarom Source Model

Microbarom source regions are modelled by applying the finite ocean atmospheric microbarom radiation source strength model as described by *Waxler et al.* [2007]. The sea state $\xi(\mathbf{x}, t)$, depending on horizontal position \mathbf{x} and time t , is described by the ECMWF ocean wave model. Altitude z is used to indicate the ocean ($z < \xi$) or atmosphere ($z > \xi$) source region, whereas D refers to the depth of the water column.

The fundamentals of the oceanic microbarom radiation model ($z < \xi$) are first described by *Longuet-Higgins* [1950], proving that the source mechanism is radiation resulting of the interaction of counter propagating ocean waves. The pressure oscillations, due to acoustic radiation, are due to second-order perturbative terms in the expansion of the fluid dynamics equations. This results in a frequency doubling with respect to the surface waves. *Longuet-Higgins* [1950] developed the fundamentals of a finite-ocean microbarom source model, for oceanic microbaroms, only many years later taken into account and applied by *Kedar et al.* [2008]. The oceanic microbarom radiation model, assuming an infinitely deep ocean, was validated by *Hasselmann* [1963]. He related the source strength density to the density of counter propagating waves for a specific frequency, known as the Hasselmann integral (H),

$$H(T) = \int_0^{2\pi} F(T, \theta) F(T, \theta + \pi) d\theta \quad (1)$$

with F ($\text{m}^2 \text{s rad}^{-1}$) the directional spectral density function, depending on the wave period T and direction θ . Note that period of the ocean wave for F is half the acoustic frequency ($T = 2/f$). The spectral density function is approximated by the discrete 2DFD of the ECMWF WAM. The oceanic microbarom radiation source strength spectrum squared is stated in equation (2) ($z < \xi$).

To simulate the atmospheric component of microbarom radiation ($z > \xi$), *Brekhovskikh et al.* [1973] extended the Longuet-Higgins microbarom source model with radiation from water into air. *Waxler and Gilbert* [2006] then refined this atmospheric component, including second-order compression of air. Finally, *Waxler et al.* [2007] assumed a finite ocean assuming an elastic sea floor, to take into account the effects of column resonance in the Longuet-Higgins and Brekhovskikh terms. The microbarom source strength spectrum squared, $D(f)$, is defined as

$$D(f) = 4g^2 \pi^4 f^3 H(T) \begin{cases} \frac{\rho_w^2}{c_w^2} \frac{A}{B} & z < \xi \\ \frac{\rho_a^2}{c_a^2} \left(\frac{9g^2}{4\pi^2 c_a^2 f^2} + \frac{c_a^2}{c_w^2} \frac{A}{B} + \frac{3g}{2\pi c_w f} \frac{C}{B} \right) & z > \xi \end{cases} \quad (2)$$

with gravity acceleration g , speed of sound c_σ , and density ρ_σ , with σ representing atmosphere (a), water (w), or seafloor (b), respectively. Coefficients A , B , and C are the resonance terms because of the finite ocean,

$$\begin{aligned} A &= \mathcal{R}^2 \cos^2(k\pi) + \sin^2(k\pi) \\ B &= \cos^2(k\pi) + \mathcal{R}^2 \sin^2(k\pi) \\ C &= (1 - \mathcal{R}^2) \sin(k\pi) \cos(k\pi) \end{aligned}$$

with constant reflection coefficient $\mathcal{R} = (\rho_w c_w) / (\rho_b c_b)$, obtained from the continuity of pressure between water and the solid seafloor.

Column resonance is determined by the frequency of the microbarom signal f and the ocean depth D , assuming the microbaroms radiate on a direct path between surface and solid-seafloor without spreading.

As microbarom signals are reflected on the solid seafloor, interaction occurs between the downward and upward propagating signals. As signals with the same frequency are combined, this results in an interference pattern caused by their superposition. The amount of interference depends of the phase difference k between the signals, with $k = 2fD/c_w$. The ocean depth is obtained from the General Bathymetric Chart of the Oceans (GEBCO) global 30 arc-second gridded bathymetry data set [Becker *et al.*, 2009], resampled using grid sample of Generic Mapping Tools [Wessel and Smith, 1991] to match the ECMWF WAM grid.

Equation (2) becomes the microbarom source model for an infinitely deep ocean, as described in the paper of Waxler and Gilbert [2006], when $\mathcal{R} = 1$ (solid seafloor is water) such that resonance terms become $A/B = 1$ and $C = 0$.

3.2. Atmospheric Propagation

Sound propagation through the atmosphere is affected by the atmosphere itself, which may result in either reflection or refraction and attenuation of the signal. The relation between density and pressure, affected by temperature (T_a), determines the speed of sound (c_a) of the medium. As the atmosphere is in motion, sound propagation is affected by the residual of the projected wind in the direction of propagation. Approximating the wave equation for infrasound in a horizontally stratified atmosphere, characterised by temperature and horizontal wind, results in the effective speed of sound c_{eff} [Gossard and Hooke, 1975]. Speed of sound, $c_a = \sqrt{\gamma RT_a}$, is defined by the ideal gas law with adiabatic conditions existing of the ratio of specific heats, for air $\gamma = c_p/c_v = 1.4$, the specific gas constant $R = 287 \text{ J kg}^{-1} \text{ K}^{-1}$, and temperature T_a depending on position and time. For a fixed horizontal position and time, c_{eff} is defined as

$$c_{\text{eff}}(z, \theta) = c_a(z) + \hat{u}_{xy}(\theta) \cdot \mathbf{w}_{xy}(z) \quad (3)$$

with $\hat{u}_{xy} \cdot \mathbf{w}_{xy}$ the projected horizontal wind in azimuth direction of the sound propagation θ at a specific altitude z . Note that all direction angles for the array processing are expressed in back-azimuth $\phi = 180 - \theta$, the arrival angle of the ray. The effective speed of sound ratio $c_{\text{eff,ratio}}$, indicating the refractivity of the atmosphere, is defined as the ratio of the effective speed of sound at an altitude z and at the ground, at equal time and location,

$$c_{\text{eff,ratio}}(z, \theta) = \frac{c_{\text{eff}}(z, \theta)}{c_{\text{eff}}(0, \theta)} \quad (4)$$

In order to have signals refracting back to the ground, the effective speed of sound ratio should be near to or greater than one. The effective speed of sound ratio is a useful indicator of infrasound propagation but does not describe the actual propagation itself.

Infrasound propagation can be described by ray tracing, e.g., [Benamou, 1995; Blom and Waxler, 2012]. In this study, a self-developed ray code is used. Rays are obtained from a high-frequency approximation of the wave equation. The wave equation, describing the disturbance of an infinitesimal volume of air in space-time, can be characterised by a surface in space-time, the Eikonal, describing only the position of the wavefront instead of the full wave [Stone and Goldbart, 2009]. Therefore, amplitudes are no longer resolved. The Eikonal operates as a high-frequency approximation, with rays spanning this characteristic surface. Applying a canonical transformation to the Eikonal results in the equations of motion, the ray equations for position and slowness.

Although ray tracing does not include amplitude information, amplitudes can be associated to each ray, described by the transport equation, based on geometrical spreading of the rays [Jensen *et al.*, 2011]. Geometrical spreading is obtained from the Jacobian determinant for ray coordinates azimuth and elevation. Atmospheric attenuation (α) includes incoherent transmission loss due to geometrical spreading from the rays and frequency dependent absorption by the atmosphere, described by Sutherland and Bass [2004]. Absorption depends variations in thermal conductivity, density, and viscosity throughout the medium and concentrations of chemical components.

Ray tracing is applied in spherical coordinates using 3-D atmospheric specifications, interpolated by cubic splines with a smooth kernel. Ray elevation angles range from 0 to 40° with steps of 1° and azimuth angles range from 0 to 358° with steps of 2°. Elevation angles larger than 40° do most likely refract beyond the stratosphere but cannot be obtained using the ECMWF analysis. A source frequency of 0.2 Hz is assumed for all rays, as this only influences the atmospheric absorption, which is rather low in for stratospheric returns

and does not vary significantly due to small changes in source frequency. Only reflection points on the ground and sea surface are stored for the simulated microbarom observations. Due to the low frequencies, rays that refract close to the surface can also result in signals observable at the ground. Therefore, rays that refract close to the surface, at maximally 1.7 km above the earth surface ($0.20 \text{ Hz} \times 340 \text{ m s}^{-1}$), will also result in a reflection point for the simulations.

3.3. Simulated Microbarom Observations

The ECMWF analysis is evaluated, using ray tracing, to identify trends in stratospheric return height ambient noise observations that cannot be explained by the analysis. A proper propagation path is described by the eigenray between a microbarom source and the array, resulting in a detectable amplitude. As many active microbarom regions can be potential microbarom sources, ray tracing is applied reversely to avoid determining all possible eigenrays of all possible source locations to the array. Using reverse ray tracing, infrasound propagation starts at the array (see Figure 1) and is propagated backward with reflection points being possible source locations. Each ray between receiver and possible source location is thus an eigenray, with the initial azimuth angle of the ray corresponding with the observed back-azimuth angle. Reverse ray tracing is acquired by modifying the atmospheric profile, thus reversing the direction of the horizontal wind and changing the sign of the horizontal components of the metrical tensor for the atmospheric derivatives used in the ray and jacobian equations. The use of reverse ray tracing with only a fixed set of rays does result in eigenrays, but these rays do not necessary correspond with the actual observed source. It is possible that a nearby, weaker source is reached.

Possible source locations, oceanic reflection points, are evaluated by a simple first-order coupling between the source and propagation model. Assume each reflection point behaves as an independent point source constant over the area S , simulated microbarom power becomes

$$A_{\text{sim}}^2 = \alpha \cdot D_a \cdot S \quad (5)$$

with the atmospheric attenuation $\alpha \text{ (m}^{-2}\text{)}$, due to spreading and absorption, and the microbarom source energy spectrum $D_a \text{ (Pa}^2 \text{ Hz}^{-1}\text{)}$.

As the source area S is unknown, the normalized simulated microbarom power can be defined as [Waxler and Gilbert, 2006]

$$\hat{A}_{\text{sim}}^2 = \alpha \cdot D_a \quad (6)$$

The simulated microbarom spectral amplitude, A_{sim} , should be equal to the observed microbarom spectral amplitude, A_{obs} , such that the required source area S holds

$$S = A_{\text{obs}}^2 / \hat{A}_{\text{sim}}^2 \quad (7)$$

From equation (7), the corresponding source radius is calculated, assuming a perfect circular source area of constant amplitude. The source radius is used to validate the plausibility of the simulations, by identifying unrealistic source dimensions. Realistic source radii are limited to 1000 km, equivalent to half the northern Atlantic Ocean.

Microbarom spectral amplitudes are interpolated in space and time to obtain the source amplitude for each oceanic reflection point. Microbarom simulations are filtered by applying the following criteria. Only oceanic reflection points with an attenuation of 60 dB RE 1 m and more are included. An attenuation smaller than 60 dB RE 1 m over a distance of $> 1000 \text{ km}$ most likely corresponds with a ray caustic, resulting in a minus infinite or unrealistically small attenuation.

4. Results

4.1. Infrasound Observations

Figure 2 shows the infrasound observations of arrays IS18 (left panes) and IS53 (right panes), respectively. Shown are processing results and array surface wind strength for the period of 1 December 2008 up to 28 February 2009. The energy spectrum shows a good correlation with the expected $0.2 \pm 0.1 \text{ Hz}$ band for microbaroms. The surface wind strength, from high-resolution sonic anemometers at the array central element, indicates the noise level at the array. Increased noise levels, resulting from strong surface winds, degrade the

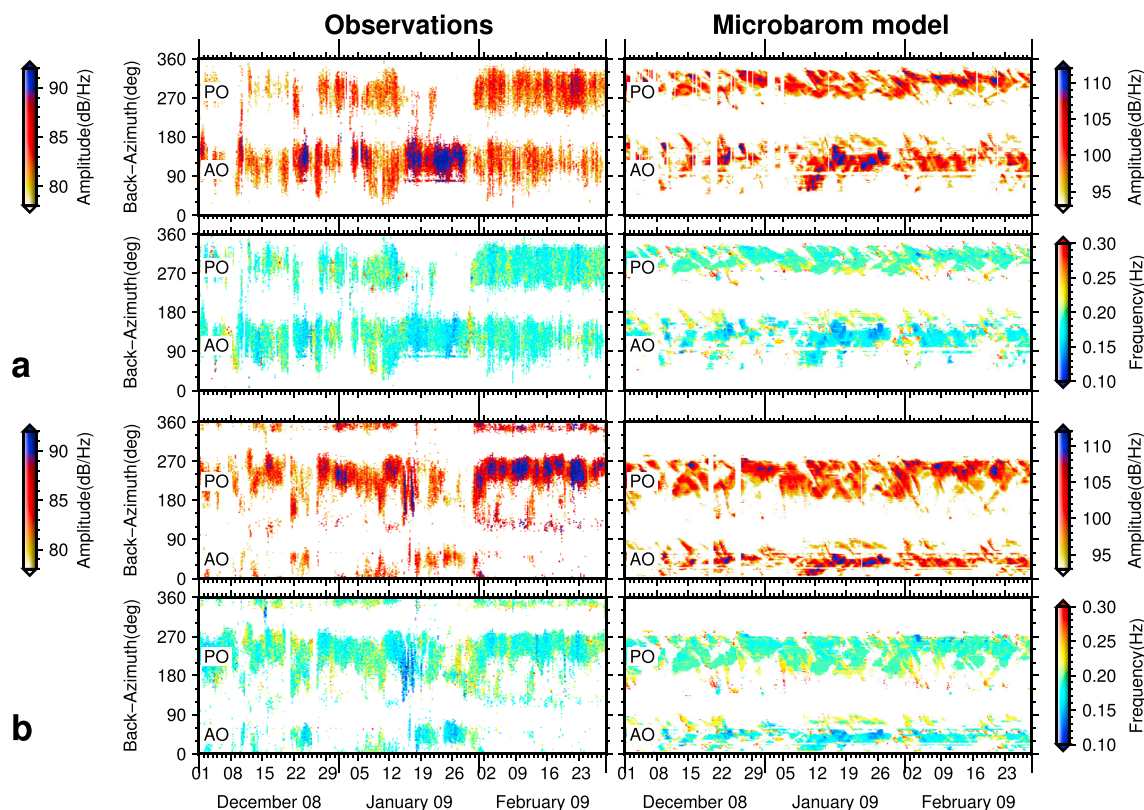


Figure 3. Comparison of the infrasound observations (left) and the microbarom source model (right), for (a) IS18 and (b) IS53, respectively. Each subfigure shows the spectral amplitude (top) with the corresponding frequency (bottom), per degree back-azimuth for each hour for the observations and for each 6 h for the microbarom source model. For the observations, the spectral amplitude corresponding to the maximum SNR is shown, and for the microbarom source model, the maximum spectral amplitude. Gaps appearing in the array processing results due to high wind noise or data loss (see Figure 2) are recreated in the microbarom source model. Microbarom source specifications are obtained from the ECMWF Wave Atmosphere Model (WAM) applying the Waxler *et al.* [2007] model for atmospheric radiation including bathymetry effects.

infrasound detectability by reducing the signal coherency over the array [Walker and Hedlin, 2009]. This can be seen in the SNR. Surface winds are inversely related with SNRs, as F is coupled to the source activity and array coherency.

Figure 3 shows the comparison of the microbarom detections with the microbarom radiation model for amplitude and frequency. The microbarom observations and the source model agree well. Despite the influence of the atmospheric propagation, there is a good resemblance between observed and simulated amplitudes and frequencies as well as between the observed SNR and modelled amplitude. For both arrays and both oceans, the back-azimuth deviation is rather small, except for weaker detections at IS53 toward the north and south-east. Detections with back-azimuth angles of $> 300^\circ$ and $120\text{--}150^\circ$ do not appear in the source model. These detections do most likely correspond with the modelled microbarom sources in Figure 3 but are affected by atmospheric propagation effects resulting in significant back-azimuth deviations and lower SNRs and amplitudes.

Table 1 presents the mean spectral amplitude, for the observations and the microbarom source model. Interesting is the difference in microbarom frequency between AO and PO, which is present in both the observations and source model. The lower frequencies for the AO can be explained by the deeper ocean, resulting in the resonance of lower frequency microbarom signals. This proves the added value of using the finite ocean microbarom source model of Waxler *et al.* [2007], allowing such bathymetry dependent variations. The observed frequencies (see Figure 3) show a relation with the direction of the stratospheric polar vortex above the array. Lowest frequencies are observed when the stratospheric duct is stable or in direction of the nearest ocean microbarom source region. IS53 in PO direction observes very low frequencies from 15 to 19 January 2009, with a broader energy spectrum. It is unclear if this is related to the microbarom source,

Table 1. Mean Microbarom Spectral Amplitude, With One Standard Deviation Range, per Ocean for the Observations and the Microbarom Source Model

	AO	PO
IS18	0.187±0.023 Hz	0.190±0.022 Hz
IS53	0.185±0.022 Hz	0.191±0.025 Hz
Model	0.189±0.031 Hz	0.200±0.021 Hz

although this does not appear in the microbarom source model, an atmospheric effect or due to wind noise at the array.

The SSW leaves a clear signature in the infrasound observations, as described by Evers and Siegmund [2009]. The back-azimuth clearly shows the direc-

tional change of the stratospheric polar vortex. Both arrays indicate a stratospheric duct to the PO in regular winter conditions, changing to a stratospheric duct to the AO during a SSW due to the SSW. This agrees with the stratospheric duct of the analysis in Figure 4. Before the warming, the stratospheric duct is unstable compared to the situation after, clearly noticeable in the SNR and energy spectrum in Figure 2. During 60 days after the onset of the warming, the stratospheric duct slowly descends into the lower stratosphere, followed by anomalous tropospheric weather regimes [Baldwin and Dunkerton, 2001]. The slow downward movement of the polar vortex is related to the offset mechanism a SSW, which is more gradually than the SSW onset [Limpasuvan et al., 2005]. The SSW onset is associated with stratospheric wind reduction anomalies produced by wave driving, which can be rapid. The SSW offset is associated with the radiative cooling of the polar cap, which happens more gradually.

Figure 4 does not explain the propagation of all observations due to the altitude limit of the analysis. IS18 almost continuously receives AO microbaroms, while IS53 almost continuously detects PO microbaroms, even when no stratospheric duct is present. During the warming, the SNR varies, increasing for the IS18 AO microbaroms and decreasing for the IS53 PO microbaroms. Interesting are the observed distant AO microbaroms around 22 December 2008 for IS53, while the analysis does not indicate the presence of a stratospheric duct. It is not yet clear if these detections, when no stratospheric duct is present, are related to the either the not resolved thermospheric ducts or an error in the analysis. Therefore, additional information on the atmospheric return height is required.

4.2. Stratospheric Versus Thermospheric Return Heights

As infrasound propagates through the atmosphere, the signal, most sensitive at the return height, is continuously influenced by the atmosphere, resulting in an integrated effect at the surface [Drob et al., 2003]. A different influence by the stratosphere and stratosphere will result in a different signature in the detections, allowing both signals to be distinguished. As the stratosphere and thermosphere are exposed differently to solar tidal fluctuations of temperature and wind, a different solar tidal signature is present in the observed microbaroms. In the stratosphere, the diurnal thermotidal oscillation is primarily excited due to water vapour heating in the troposphere. This remains true until the thermosphere, where viscosity, conductivity, and electromagnetic damping may attenuate incoming waves [Lindzen and Chapman, 1969]. The thermospheric

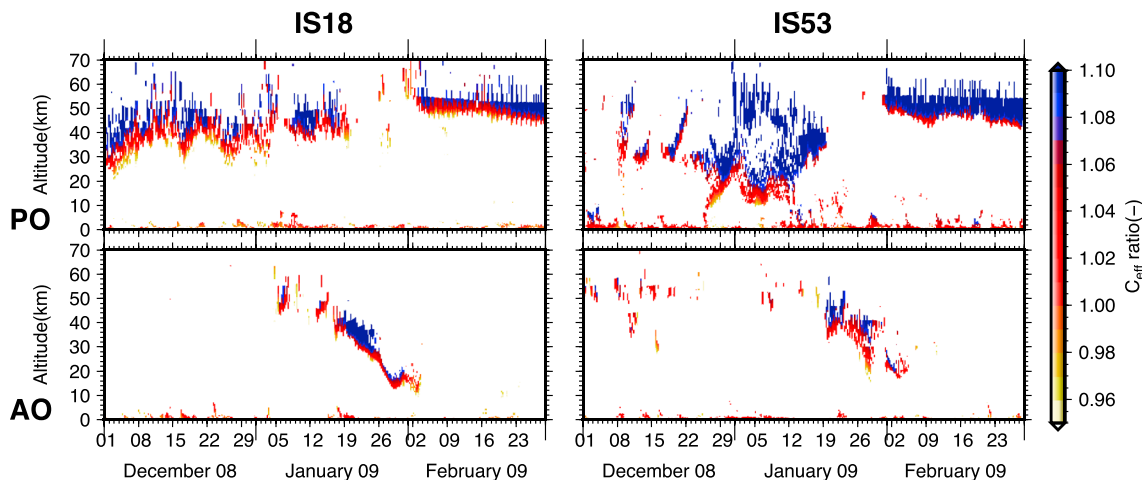


Figure 4. Effective speed of sound ratio for arrays (left) IS18 and (right) IS53 for mean back-azimuth direction toward the Pacific Ocean (top) and the Atlantic Ocean (bottom).

is characterized by a high attenuating nature caused by the low density [Sutherland and Bass, 2004]. Therefore, thermospheric semidiurnal solar tides are excited to a greater degree due to the heat generated by the absorption of solar ultraviolet radiation by oxygen around 120 km altitudes. Irregular heating of the atmosphere results in a variation of the thermospheric return height, twice a day, due to the change in wind strength and attenuation.

The typical signature is represented in the detection characteristics, for example, the number of detections, back-azimuth angle, apparent velocity, bandwidth, and amplitude [Le Pichon et al., 2005; Whitaker and Mutschlechner, 2008; Green et al., 2012]. Assink et al. [2012] looked at travel time variations and its relation to return height variations associated with atmospheric tides. All studies make use of strong impulsive sources with a well known position, e.g., volcanoes, which makes it hard to implement the used methodologies on ambient noise. The studies of Donn and Rind [1971], Rind et al. [1973], and Rind and Donn [1975], Rind [1978] statistically relate observed microbarom amplitudes to solar tidal fluctuations using the mean amplitude per time of day (tod), \bar{A}_{tod} . However, the presented method involves long-period averaging, using several months of data, losing all small scale fluctuations of interest. Therefore, \bar{A}_{tod} is calculated for each day.

Atmospheric tides are found in the daily normalized spectral powers (see Figure 5) obtained from the best-beam peak spectral amplitudes in direction of the AO and PO for IS18 and IS53, respectively. For each half hour (one pixel), consisting of at least 15 detections with a SNR of 1.5 and more for IS18 and of 1.3 and more for IS53, the peak spectral power is averaged. The mean spectral amplitude per time of day (tod), \bar{A}_{tod} , in direction of the AO and PO, is computed following a method similar to the method described by Donn and Rind [1971]. Variations in the directional daily mean amplitude \bar{A}_{day} , shown below the normalized spectral powers, are in agreement with the expected return heights from the solar tidal signature. Higher daily mean amplitudes are observed for expected stratospheric return heights; for example, see Figure 5b in January during the SSW. The color coded horizontal bar in Figure 5 roughly indicates periods with either diurnal or semidiurnal signatures, manually picked.

\bar{A}_{tod} for IS18 shows a clear semidiurnal variation in direction of the AO (Figure 5b), in agreement with Donn and Rind [1971], indicating mainly thermospheric return heights. A similar semidiurnal signature is shown by the normalized spectral powers, with periods in agreement with the lack of a stratospheric duct indicated by c_{eff} . In December, when the stratospheric duct is unstable, scattered signals are observed resulting in an unclear rather semidiurnal signature. When the AO duct becomes stratospheric, indicated by the green periods, the tidal signature becomes diurnal, with stronger daily mean amplitudes \bar{A}_{day} . After the warming, the atmosphere stabilizes resulting in a clear semidiurnal signature up to halfway February. From then on, the number of detections decreases too much to clearly determine the tidal signature. In PO direction, the dominant signature is diurnal. In December, during the unstable stratospheric duct, the signature is very vague. After the warming, during the first half of February 2009, a weaker peak around 18 h can be observed as well. This signature is most likely related to the interactions of the stratospheric and thermospheric tides, corresponding to mixed stratospheric-thermospheric propagation. In the modelling, described in the next subsection, these mixed propagation paths will be missing, similar to the detections related to pure thermospheric return heights.

\bar{A}_{tod} for IS53 in PO direction indicates a diurnal signature. The daily normalized power reveals significant phase variations of the diurnal signature during the 3 month period. A weak semidiurnal signature is present in early December 2008, which is in agreement with the lack of a stable stratospheric duct in Figure 4. In AO direction \bar{A}_{tod} indicates a less pronounced diurnal signature. However, the signature becomes more clear for the normalized power, indicating a clear stratospheric duct at the time of the warming, in agreement with c_{eff} . The IS53 AO detections around 22 December 2008 show a diurnal signature with a maxima around 16 h (see Figure 5d), indicating a missing stratospheric duct in the analysis.

Interesting is the phase reversal of the IS53 AO diurnal maximum from approximately 20 h for 17 to 21 January 2009 to approximately 4 h for 23 to 28 January 2009. The reversed phase takes place during the vortex split of the stratospheric polar vortex with a significant directional change of the stratospheric wind. Due to the vortex split, the flow changes significantly but does not completely reverse. Consequentially, the AO duct changes, moving south, resulting in a phase change of the diurnal peak. Therefore, a phase change of the diurnal signal is an indicator of a significant directional change of the stratospheric vortex. A similar phenomena can be denoted at IS18 in AO direction. During the vortex split, the tidal signature becomes

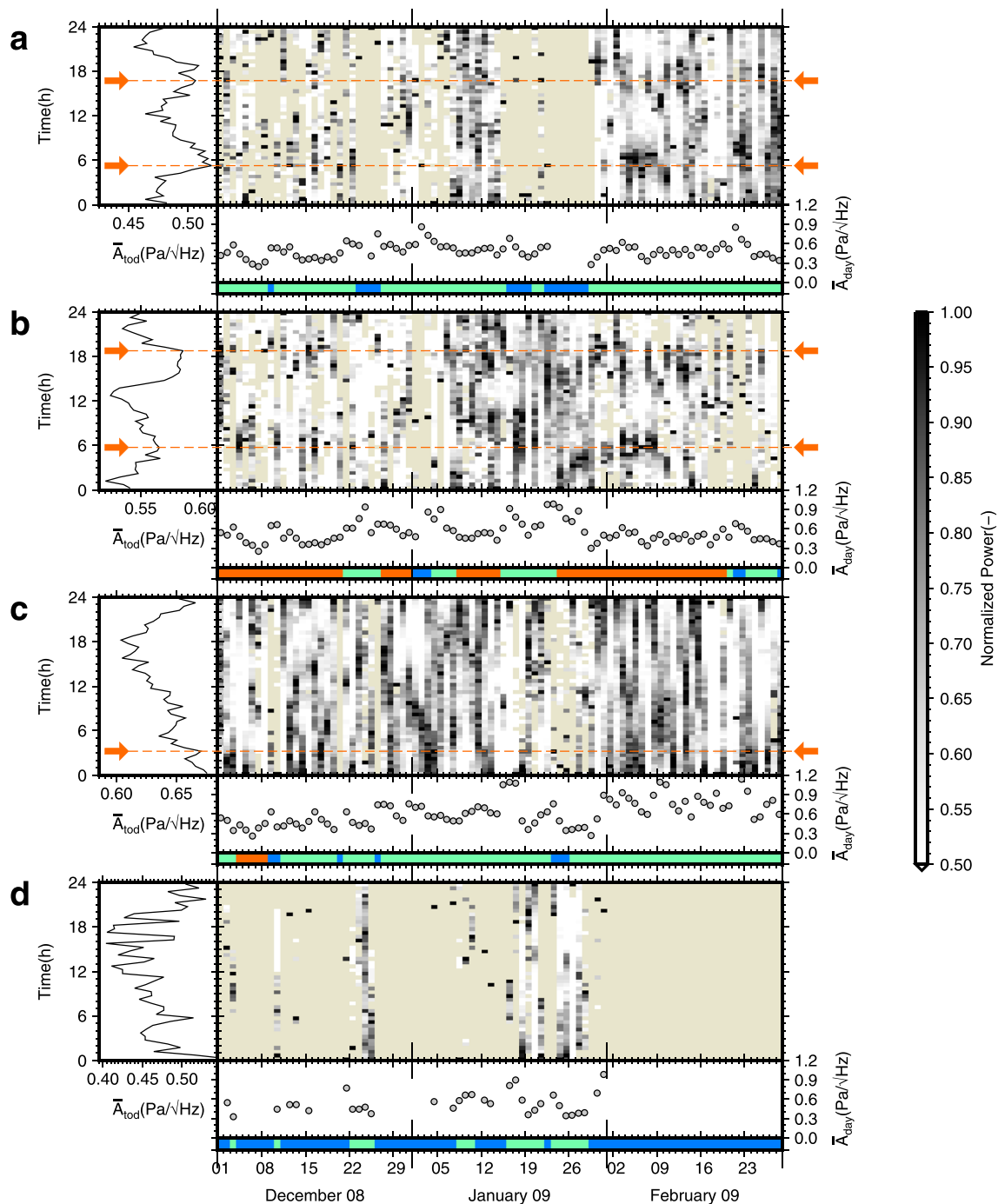


Figure 5. Directional time averaged spectral amplitude variations. From top to bottom are shown IS18 in direction of the (a) Pacific Ocean and (b) Atlantic Ocean, IS53 in direction of the (c) Pacific Ocean and (d) Atlantic Ocean, respectively. Each subfigure consists of a vertical graph (left) and an image (right) with below one horizontal graph and one colour coded bar. The vertical graph (left) shows the spectral amplitude averaged per time of day, \bar{A}_{tod} , for each half hour. The red arrows and dashed lines indicate the tidal peaks in the mean time of day amplitude, if present. The image (right) shows the half hour averaged spectral power, normalized per day. Each pixel column corresponds with one single day, while each row indicates the time of day. The horizontal graph shows the daily mean spectral amplitude \bar{A}_{day} . The colour coded bar roughly indicates manually picked periods with either no peak (blue), one peak (green) or two peaks (red) per day, respectively. Only detections are used with $SNR \geq 1.5$ for IS18 and $SNR \geq 1.3$ for IS53.

semidiurnal, but less clear than after the SSW indicating a mixed stratospheric–thermospheric path, with a constant phase change due to the continuing directional change of the stratospheric wind.

4.3. Simulated Microbaroms Observations

Microbaroms observations are simulated to verify the analysis with the expected stratospheric returns resulting from the spectral amplitude variations. Because the atmosphere is a 4-D problem (3-D position and time), 3-D reverse ray tracing is used with 6 h discrete time steps, assuming the atmosphere is constant along this period, to determine source locations. This implicates a similar behaviour of the mean observed signal for this time window. The microbarom source model of *Waxler et al.* [2007] is used to filter out likely source locations, using to source amplitude, then validated calculating the required source area as described in 3.3.

The proposed simulation consists of limitations in both the used data as the methodology applied. A major limitation of the data is the vertical limit of the analysis. Therefore, thermospheric and combined stratospheric-thermospheric signals cannot be resolved. Ray tracing has some limitations as well. First of all, the limited number of rays spanning the wavefront results in a decreasing resolution with distance. As a result, some source regions cannot be reached, or correspond with a weaker microbarom region. Second, rays can become chaotic over very long distances, resulting in an unrealistic large attenuation. Finally, ray tracing is affected by caustics, resulting in singularities, enforced by the use of a 3-D atmospheric profile due to the increased number of directional changes of rays compared with 1-D ray tracing. The assumption of independent microbarom sources behaving as a point source with a circular area S will probably underestimate of the radiated microbarom signals, resulting into too low observed amplitudes.

Microbarom simulations for IS18 (see left-hand side of Figure 6) can be explained by two phases: before the SSW and from the warming onward. Before the SSW, only a sparse number of simulations in both AO and PO direction are obtained. This is as expected due to the semidiurnal signature present in AO direction and a weaker signature for the PO with an unstable and too northerly stratospheric duct, resulting in unresolved thermospheric and mixed stratospheric-thermospheric paths. From the warming onward, the correlation with the observations improves. Detections with an expected stratospheric return can be propagated using 3-D ray tracing and the ECMWF analysis, in AO direction during and in PO direction after the warming, respectively. The detections with the assumed thermospheric return, in AO direction after the warming, are missing as expected. The density of the obtained PO simulations is low compared with the observations, which is most likely due to the too low number of rays. The most distant sources correspond with the very large attenuations and low source amplitudes compared with the peak source amplitude of Figure 3. This implies that ray chaos is present. During the warming, the closer AO is sampled much better, with the same number of rays, and results in more realistic simulated amplitudes. Both the back-azimuth and the amplitudes of the stratospheric detections are in agreement with the observations. Two clear differences can be denoted that can be related to possible errors in the analysis. First, during the warming, from 14 to 21 January 2009, many too northerly simulations are present. From the observations, it holds that the warming onset and corresponding change of stratospheric polar vortex is much faster than in the ECMWF model, resulting in a clearer switch from PO to AO duct. Second, at the end of February the analysis tends to deviate slightly southerly, while the observations do not show this deviation. Simulations tend to be too much constrained by the direction of the circumpolar vortex compared with the observations, indicating an offset in the direction of stratospheric polar vortex in the analysis.

Simulations for IS53 (see right-hand side of Figure 6) show in general good agreement with the observations, as propagation is dominated by stratospheric return heights. Before the warming, the simulation is similar to IS18. The unstable stratospheric duct in PO direction results in only a few stratospheric simulations who do not reach the active microbarom areas. Although this unstable stratospheric, observations with back-azimuth angles of $>330^\circ$ are present, indicating the added value of 3-D propagation. After the warming, when the stronger and more constant stratospheric duct is more westerly, these signals are missing. Only AO, stratospheric, simulations are present during the SSW as expected, with the exception of 22 December 2008. Although a clear stratospheric duct is present (see Figure 5), no stratospheric returns can be simulated. The simulations in AO direction from 19 January onward tend to be different from the observations, which are closer concentrated between 30° and 60° back-azimuth. Despite the very high attenuation for these simulations, it seems that the core of the microbarom source region is reached, indicated by high source amplitudes. As these directions are in agreement with the observed amplitudes, the analy-

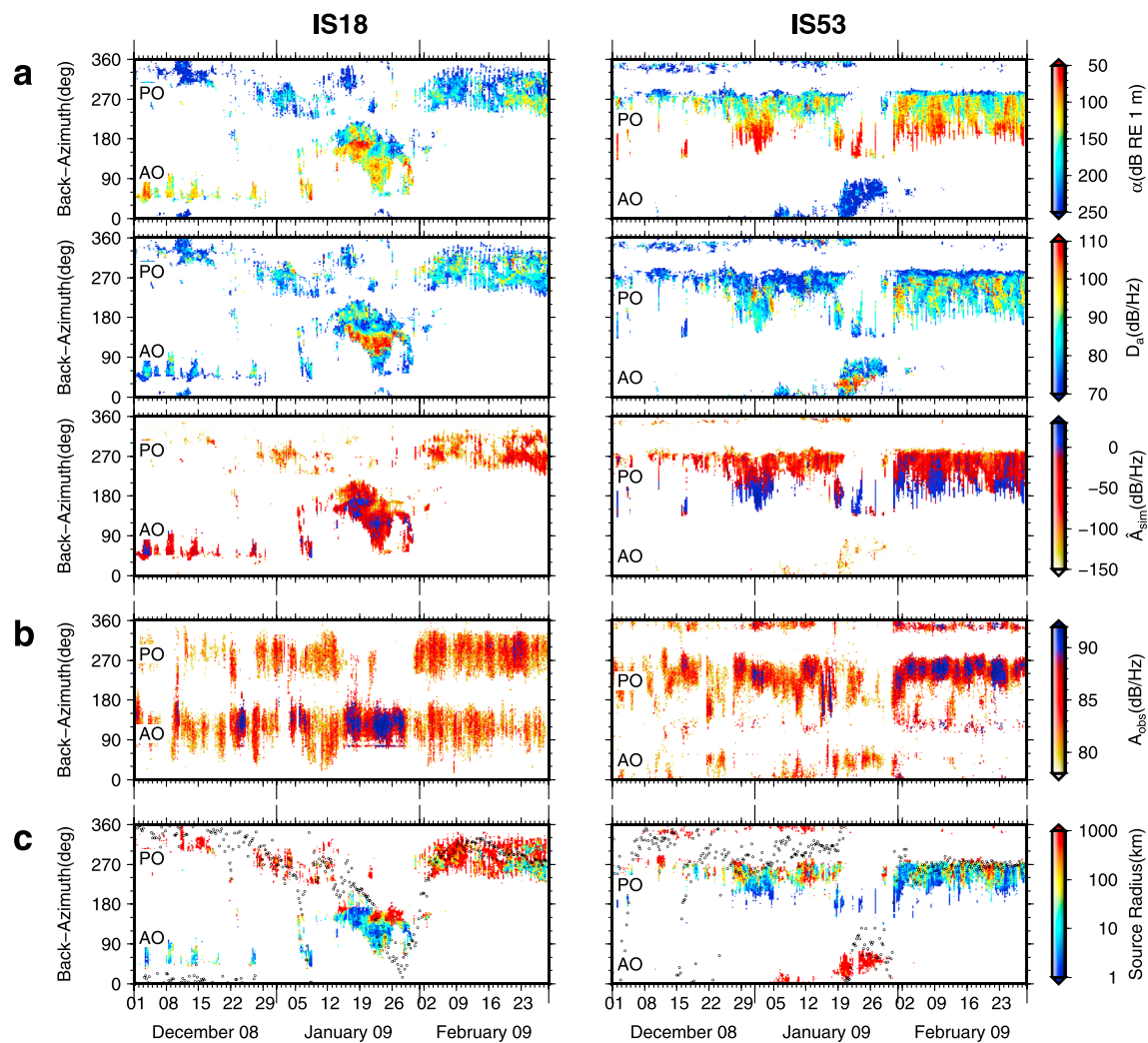


Figure 6. Results of the microbarom simulations (Figure 6a) compared with the observed peak SNR spectral amplitudes (Figure 6b) and the required source radius (Figure 6c) of IS18 (left) and IS53 (right) per back-azimuth angle in time, respectively. (a) Colour coded are, from top to bottom, attenuation, source spectral amplitude, and simulated received spectral amplitude. (b) Observed amplitudes as shown in Figure 3. (c) Required source radius, with black dots representing the wind direction at 50 km altitude above the array derived from the ECMWF HRES analysis.

sis performs well during the warming. At the SSW offset, from 26 January 2009 onward, a small, increasing, back-azimuth deviation between simulations and observations occurs indicating a possible error. At the beginning of February 2009, the observed AO signals are missing in the simulations.

5. The Life Cycle of a SSW

The differences between the observed and simulated expected stratospheric return heights are mostly related with the SSW, indicating the loss of performance of the analysis due to the sudden warming. Most important is the completely missing stratospheric return height AO detections of IS53 at 22 December 2008 using the analysis. Also, during the warming halfway January 2009, the directional change of observed microbaroms for IS18 is much faster and from the opposite direction (northward instead of southward) than shown by the ECMWF analysis.

The analysis indicates a displaced westerly elongated vortex from 18 to 22 January 2009 and a vortex split from 24 to 28 January 2009, corresponding with two stratospheric vortices, followed by a recovery of until 4 February 2009. First signatures of the warming are indicated by small variations around 22 December 2008 and 7–8 January 2009. Hemispheric 10 hPa (~31 km) wind analysis before, during, and after the SSW can be

found in the supporting information, clarifying the evolution of the stratospheric polar vortex during the 2009 SSW.

Figure 5 reveals additional information about the life cycle of the warming. The effect of the warming is most pronounced for IS53 as AO microbaroms with a $SNR \geq 1.3$ (see Figure 5d) are only expected in summer or in case of a SSW. Therefore, IS53 is used to describe the life cycle of the warming due to the clearest signature. Observations reveal more abrupt changes, increasing in intensity and duration, and some differences in the onset and offset. Largest differences are the very clear AO stratospheric duct from 22 to 25 December 2008, completely missing in the analysis, indicating a vortex disturbance, and an earlier stratospheric vortex recovery, at 30 January 2009. The series of abrupt changes can be explained by Rossby wave breaking in the stratospheric polar vortex. Rossby waves, type 2 planetary, have a typical period of 10 to 16 days [Holton, 2004]. In winter, these waves can be forced up into the stratosphere, disturbing the circumpolar vortex via momentum dumping. At the beginning of the winter, in December 2008, the circumpolar vortex is strong but highly unstable, being very sensitive to any disturbance. Therefore, it is triggered easily by the Rossby wave breaking, resulting in first signatures on 3 and 10 December 2008, and is rather weak and short, observable in the short periods with low spectral amplitudes in Figure 5d. As the vortex is not yet critically disturbed, the energy balance is restored fast. As the life cycle intensifies due to the repeated wave breaking, the stratospheric vortex weakens, resulting in more extended signatures [Limpasuvan *et al.*, 2004]. This can be denoted from 22 to 25 December 2008, where a clear AO stratospheric duct is present with peak amplitudes at approximately 16 h. Because the stratospheric vortex is not yet fully disturbed, still PO detections and simulations are present. Therefore, the stratospheric vortex recovers fast. On 8–9 January 2009, very small disturbances can be denoted, in agreement with the period of Rossby waves, differing from the analysis. The westerly vortex intensifies but displaces slightly as it becomes unstable. A stronger longer lasting disturbance takes place from 17 to 21 January 2009 with a displaced and elongated but rather unstable westerly polar vortex. This results in a stratospheric duct in AO direction and a diurnal maximum at approximately 14 hours. The stratospheric vortex, highly disturbed, elongates even more until it splits into two stratospheric vortices from 23 to 28 January 2009, located above Canada and Russia. Due to the location of the vortices, no clear difference in back-azimuth is observed. However, a signature of the split can be observed by the loss of the weak PO observations for IS18 and IS53, while the AO shows an amplitude and SNR variation for IS18 and a silence for IS53. This directional change can be denoted as well from the phase change of the diurnal signature, which changes from approximately 20 to 4 h for IS53, due to the different path of the infrasound through the atmosphere. The vortex split is clearly denotable in the tidal signature of IS18 in AO direction, which is diurnal during the elongated displaced phase and changes to mixed diurnal and semidiurnal due to the vortex split. Because the two vortices displaces the semidiurnal peaks vary from 2 to 6 h and from 15 to 18 h, approximately. These vortices dissolve at the end of January 2009, resulting in a normal winter situation. Because of the weak polar vortex, recovering slowly due to the gradually radiative cooling of the polar cap [Limpasuvan *et al.*, 2005], a stable continuous stratospheric duct in PO direction is present, clearly noticeable in the microbarom observations.

6. Discussion and Conclusions

In this study, a method is presented to study the life cycle of a SSW using infrasonic ambient noise observations. The 2009 major SSW is used as a case study because of its very clear influence on infrasound propagation [Evers and Siegmund, 2009].

It is shown that the implemented Waxler *et al.* [2007] microbarom amplitude density model with bathymetry, using the ECMWF WAM coupled ocean–atmosphere model input, explains very well the observed microbaroms. The microbarom source model resolves observed ocean depth frequency difference, resulting in slightly lower frequency AO microbaroms. Therefore, infrasound ambient noise is an excellent source to probe the upper atmosphere that can be modelled well. Knowledge of the atmospheric ducting condition of the observed microbaroms is obtained from the infrasonic amplitudes, without any a priori atmospheric information. It is successfully shown that spectral amplitude variations of continuous microbarom observations can reveal whether the sound propagated through the stratosphere or thermosphere, based on the diurnal or semidiurnal signature. These findings are verified by simulations, using 3-D reverse ray tracing and the microbarom source model, with the known implications of a vertically limited atmospheric model. Although these limitations, regions of stratospheric propagation can be identified, confirming the amplitude variations method. Thermospheric signals of IS18 toward Atlantic Ocean, with

distance of 2000 up to 3500 km (February 2009), can be observed. This study shows the use of microbarom observations to validate the state of the atmosphere represented by the ECMWF analysis, indicating in general a good agreement but with clear differences dedicated to the SSW. It is shown that infrasound can provide additional information of the state of the atmosphere, with the potential to contribute to NWP, especially in case of a SSW. A vortex displacement and a vortex split leave a clear signature in the infrasound observations, resulting a solar tidal signature type and or phase variation, which can be distinguished from each other. Maybe in the future infrasound can assist AMSU-A observations to force the first-guess field more toward the actual state of the rapidly varying atmosphere. The observed microbarom amplitudes show more details on the SSW life cycle, with differences in the warming onset and offsets, than present in the ECMWF analysis. Simulations are over constraint by the direction of the circumpolar vortex, whereas observations indicate some differences.

Some further investigation is required. Errors in array processing of simultaneous coherent signal detection, more specific the spectral amplitude estimate, have a significant impact on the amplitude variation method. Errors in separating AO from PO microbarom observations can lead to in errors in the amplitude variations and thus tides. Although a larger window for the spectral analysis, filled with zeros, is used to minimize this problem, still other signals can be present in the best-beam, affecting the SNR. The assumption that each reflection point behaves as an independent source, which is constant over area S , works to evaluate the plausibility of the obtained eigenrays but is rather unrealistic. A more realistic approach is presented by Waxler and Gilbert [2006], using the cross spectral density from Greens function as propagation factor for the microbaroms. Infrasound propagation can be improved by simply increasing the number of rays significantly, or by iteratively determining the eigenrays for all strong source regions. The use of another atmospheric propagation model that can resolve amplitudes, for example, PE or normal-mode, can improve the quality of the validation of the analysis. Some missing stratospheric return heights, assumed to be related to errors in the analysis, can probably be related to fine-scale structure in the wind and temperature and internal gravity waves generating additional arrivals [Kulichkov *et al.*, 2010; Revelle, 2010; Chunchuzov *et al.*, 2011] but are not resolved by the global circulation models as these are below the model resolution.

Acknowledgments

This work was performed during the course of the ARISE design study (<http://arise-project.eu>), funded under the Seventh Framework Programme (FP7) of the European Union (grant 284387). The data for this paper from CTBTO and ECMWF cannot be released, as they are available to member states only. Infrasound data can be requested at the International Data Centre (IDC) in Vienna, via the virtual Data Exploration Centre (vDEC). Atmosphere and ocean data can be requested at the ECMWF via the Meteorological Archival and Retrieval System (MARS), free of charge for Member States and Co-operating States, as well as some data sets for research purpose only. Many thanks to Anton Van Geyt and Julius Fricke (KNMI) for all the discussions and help in deriving the ray and Jacobian equations. Thanks to Adrian Simmons (ECMWF) for all fruitful comments improving this paper. We thank J. D. Assink, R. Whitaker, and an anonymous reviewer for their reviews which helped in improving the manuscript. We thank the CTBTO and station operators are for guaranteeing the high quality of the infrasound data. Figures in this article were made with the Generic Mapping Tools [Wessel and Smith, 1991].

References

- Andrews, D. G., C. B. Leovy, and J. R. Holton (1987), *Middle Atmosphere Dynamics*, Int. Geophys., vol. 40, Academic Press, London, U. K.
- Assink, J. D., R. Waxler, and D. Drob (2012), On the sensitivity of infrasonic traveltimes in the equatorial region to the atmospheric tides, *J. Geophys. Res.*, *117*, D011110, doi:10.1029/2011JD016107.
- Assink, J. D., R. Waxler, P. Smets, and L. G. Evers (2014), Bidirectional infrasonic ducts associated with sudden stratospheric warming events, *J. Geophys. Res. Atmos.*, *119*, 1140–1153, doi:10.1002/2013JD021062.
- Baldwin, M. P., and T. J. Dunkerton (2001), Stratospheric harbingers of anomalous weather regimes, *Science*, *294*, 581–584.
- Becker, J. J., et al. (2009), Global bathymetry and elevation data at 30 arc seconds resolution: SRTM30 PLUS, *Mar. Geod.*, *32*, 355–371.
- Benamou, J.-D. (1995), Big ray tracing: Multivalued travel field computation using viscosity solutions of the Eikonal equation, *Tech. Rep.*, Unité de recherche INRIA Rocquencourt, Le Chesnay Cedex, France.
- Blom, P., and R. Waxler (2012), Impulse propagation in the nocturnal boundary layer: Analysis of the geometric component, *J. Acoust. Soc. Am.*, *131*, 3680–3690.
- Brekhovskikh, I. M., V. V. Goncharov, V. M. Kurtepov, and K. A. Naugol'nykh (1973), The radiation of infrasound into the atmosphere by surface waves in the ocean, *J. Fluid Mech.*, *9*, 899–907.
- Chao, W. C. (1985), Sudden stratospheric warmings as catastrophes, *J. Atmos. Sci.*, *42*, 1631–1646.
- Charlton, A. J., and L. M. Polvani (2007), A new look at stratospheric sudden warmings. Part I: Climatology and modeling benchmarks, *J. Clim.*, *20*, 449–469.
- Charney, J. G., and P. G. Drazin (1961), Propagation of planetary-scale disturbances from the lower into the upper atmosphere, *J. Geophys. Res.*, *66*, 83–109.
- Chunchuzov, I. P., S. N. Kulichkov, O. E. Popov, R. Waxler, and J. Assink (2011), Infrasound scattering from atmospheric anisotropic inhomogeneities, *Izv. Atmos. Oceanic Phys.*, *47*, 540–557.
- Dahlman, O., P. Mykkeltveit, and H. Haak (2009), Monitoring technologies, in *Nuclear Test Ban*, chap. 2, pp. 1–34, Springer, Dordrecht, Netherlands.
- Donn, W. L., and D. Rind (1971), Natural infrasound as an atmospheric probe, *Geophys. J. R. Astron. Soc.*, *26*, 111–133.
- Drob, D. P., J. M. Picone, and M. Garcés (2003), Global morphology of infrasound propagation, *J. Geophys. Res.*, *108*(D21), 4680, doi:10.1029/2002JD003307.
- ECMWF (2009), IFS documentation Cy33r1 operational implementation 3 June 2008. Part VII: ECMWF wave model, *Tech. Rep.*, European Centre for Medium-Range Weather Forecasts, Reading, England.
- Evers, L. G., and P. Siegmund (2009), Infrasonic signature of the 2009 major sudden stratospheric warming, *Geophys. Res. Lett.*, *36*, L23808, doi:10.1029/2009GL041323.
- Evers, L. G., A. R. J. van Geyt, P. Smets, and J. T. Fricke (2012), Anomalous infrasound propagation in a hot stratosphere and the existence of extremely small shadow zones, *J. Geophys. Res.*, *117*, D06120, doi:10.1029/2011JD017014.
- Garcés, M., M. Willis, C. Hetzer, A. Le Pichon, and D. Drob (2004), On using ocean swells for continuous infrasonic measurements of winds and temperature in the lower, middle, and upper atmosphere, *Geophys. Res. Lett.*, *31*, L19304, doi:10.1029/2004GL020696.
- Gerber, E. P., C. Orbe, and L. M. Polvani (2009), Stratospheric influence on the tropospheric circulation revealed by idealized ensemble forecasts, *Geophys. Res. Lett.*, *36*, L24801, doi:10.1029/2009GL040913.

- Gossard, E. E., and W. H. Hooke (1975), Waves in the atmosphere: Atmospheric infrasound and gravity waves—Their generation and propagation, *Atmos. Sci.*, *2*, 470.
- Green, D. N., R. S. Matoza, J. Vergoz, and A. Le Pichon (2012), Infrasound propagation from the 2010 Eyjafjallajökull eruption: Investigating the influence of stratospheric solar tides, *J. Geophys. Res.*, *117*, D21202, doi:10.1029/2012JD017988.
- Gutenberg, B. (1939), The velocity of sound waves and the temperature in the stratosphere in southern California, *Bull. Am. Meteorol. Soc.*, *20*, 192–201.
- Hasselmann, K. (1963), A statistical analysis of the generation of microseisms, *Rev. Geophys.*, *1*, 177–210.
- Hedlin, M. A. H., B. Alcoverro, and G. D'Spain (2003), Evaluation of rosette infrasonic noise-reducing spatial filters, *J. Acoust. Soc. Am.*, *114*, 1807–1820.
- Hedlin, M. A. H., D. Drob, K. Walker, and C. de Groot-Hedlin (2010), A study of acoustic propagation from a large bolide in the atmosphere with a dense seismic network, *J. Geophys. Res.*, *115*, B11312, doi:10.1029/2010JB007669.
- Holton, J. R. (2004), *An Introduction to Dynamic Meteorology*, 4th ed., Elsevier Acad. Press, Oxford.
- Jensen, F. B., W. A. Kuperman, M. B. Porter, and H. Schmidt (2011), *Computational Ocean Acoustics (Modern Acoustics and Signal Processing)*, 2nd ed., Springer, New York.
- Kedar, S., M. Longuet-Higgins, F. Webb, N. Graham, R. Clayton, and C. Jones (2008), The origin of deep ocean microseisms in the North Atlantic Ocean, *Proc. R. Soc. A*, *464*(2091), 777–793.
- Kodera, K., H. Mukougawa, and A. Fujii (2013), Influence of the vertical and zonal propagation of stratospheric planetary waves on tropospheric blockings, *J. Geophys. Res. Atmos.*, *118*, 8333–8345, doi:10.1002/jgrd.50650.
- Kulichkov, S. N., I. P. Chunchuzov, and O. I. Popov (2010), Simulating the influence of an atmospheric fine inhomogeneous structure on long-range propagation of pulsed acoustic signals, *Izv. Atmos. Oceanic Phys.*, *46*(1), 60–68.
- Landès, M., L. Ceranna, A. Le Pichon, and R. S. Matoza (2012), Localization of microbarom sources using the IMS infrasound network, *J. Geophys. Res.*, *117*, D06102, doi:10.1029/2011JD016684.
- Le Pichon, A., E. Blanc, D. Drob, S. Lambotte, J. X. Dessa, M. Lardy, P. Bani, and S. Vergnolle (2005), Infrasound monitoring of volcanoes to probe high-altitude winds, *J. Geophys. Res.*, *110*, D13106, doi:10.1029/2004JD005587.
- Le Pichon, A., E. Blanc, and A. Hauchecorne (Eds.) (2010), *Infrasound Monitoring for Atmospheric Studies*, 1st ed., Springer, Dordrecht, Netherlands.
- Limpasuvan, V., D. W. J. Thompson, and D. L. Hartmann (2004), The life cycle of the Northern Hemisphere sudden stratospheric warmings, *J. Clim.*, *17*, 2584–2596.
- Limpasuvan, V., D. L. Hartmann, D. W. J. Thompson, K. Jeev, and Y. L. Yung (2005), Stratosphere-troposphere evolution during polar vortex intensification, *J. Geophys. Res.*, *110*, D24101, doi:10.1029/2005JD006302.
- Lindzen, S. R., and S. Chapman (1969), Atmospheric tides, *Space Sci. Rev.*, *10*, 3–188.
- Longuet-Higgins, M. S. (1950), A theory of the origin of microseisms, *Department of Geodesy and Geophysics, University of Cambridge*, 243.
- Matsuno, T. (1971), A dynamical model of the stratospheric sudden warming, *J. Atmos. Sci.*, *28*, 1479–1494.
- McInturff, R. M. (1978), *Stratospheric Warmings: Synoptic, Dynamic and General-Circulation Aspects*, NASA Reference Publication, vol. 1017, National Aeronautics and Space Administration, Scientific and Technical Information Office, Washington.
- Melton, B. S., and L. F. Bailey (1957), Multiple signal correlators, *Geophysics*, *22*, 565–588.
- Muench, H. S. (1965), On the dynamics of the wintertime stratosphere circulation, *J. Atmos. Sci.*, *22*, 349–360.
- Ramaswamy, V., et al. (2001), Stratospheric temperature trends: Observations and model simulations, *Rev. Geophys.*, *39*, 71–122.
- Revelle, D. O. (2010), Modified ray-mode (phase) theory: Understanding counter-wind propagation effects from atmospheric explosions, *J. Atmos. Sol. Terr. Phys.*, *72*, 241–261.
- Rind, D. (1978), Investigation of the lower thermosphere results of ten years of continuous observations with natural infrasound, *J. Atmos. Terr. Phys.*, *40*, 1199–1209.
- Rind, D., and W. L. Donn (1975), Further use of natural infrasound as a continuous monitor of the upper atmosphere, *J. Atmos. Sci.*, *32*, 1694–1704.
- Rind, D., W. L. Donn, and E. Dede (1973), Upper air wind speeds calculated from observations of natural infrasound, *J. Atmos. Sci.*, *30*, 1726–1729.
- Rind, D. H., and W. L. Donn (1978), Infrasound observations of variability during stratospheric warmings, *J. Atmos. Sci.*, *35*, 546–553.
- Shaw, T. A., and T. G. Shepherd (2008), Atmospheric science: Raising the roof, *Nat. Geosci.*, *1*, 12–13.
- Stone, M., and P. Goldbart (2009), *Mathematics for Physics: A Guided Tour for Graduate Students*, 1st ed., Cambridge Univ. Press, Cambridge.
- Stopa, J. E., K. F. Cheung, M. A. Garcés, and N. Badger (2012), Atmospheric infrasound from nonlinear wave interactions during Hurricanes Felicia and Neki of 2009, *J. Geophys. Res.*, *117*, C12017, doi:10.1029/2012JC008257.
- Sutherland, L. C., and H. E. Bass (2004), Atmospheric absorption in the atmosphere up to 160 km, *J. Acoust. Soc. Am.*, *115*, 1012.
- Walker, K. T. (2012), Evaluating the opposing wave interaction hypothesis for the generation of microbaroms in the eastern North Pacific, *J. Geophys. Res.*, *117*, C12016, doi:10.1029/2012JC008409.
- Walker, K. T., and M. A. H. Hedlin (2009), A review of wind-noise reduction methodologies, in *Infrasound Monitoring for Atmospheric Studies*, chap. 5, pp. 141–182, Springer, Dordrecht, Netherlands.
- Waxler, R., and K. E. Gilbert (2006), The radiation of atmospheric microbaroms by ocean waves, *J. Acoust. Soc. Am.*, *119*, 2651.
- Waxler, R., K. Gilbert, C. Talmadge, and C. Hetzer (2007), The effects of the finite depth of the ocean on microbarom signals, *8th International Conference on Theoretical and Computational Acoustics (ICTCA)*, Crete, Greece.
- Wessel, P., and W. H. F. Smith (1991), Free software helps map and display data, *Eos Trans. AGU*, *72*(41), 441–446.
- Whitaker, R. W., and J. P. Mutschlecner (2008), A comparison of infrasound signals refracted from stratospheric and thermospheric altitudes, *J. Geophys. Res.*, *113*, D08117, doi:10.1029/2007JD008852.